Composite Structures 266 (2021) 113740

Contents lists available at ScienceDirect

Composite Structures

journal homepage: www.elsevier.com/locate/compstruct

# The effect of sizing optimization on the interface between high strength steel and fiber reinforced composite

Fatima Ghassan Alabtah, E. Mahdi *

*Department of Mechanical and Industrial Engineering Qatar University, P.O. Box 2713, Doha, Qatar*

ARTICLE INFO

*Keywords:*
Fracture toughness
Interface
Fiber orientation
Fiber types
Steel
Stress intensity factors

ABSTRACT

This paper aims to examine fiber type and fiber orientation's effects on the interface bonding between steel and fiber-reinforced composites. To this end, fracture loads for modes I and II were experimentally determined. Three different composites were used: glass fibers/epoxy (GFRP), carbon fibers/epoxy (CFRP), and Kevlar fibers/epoxy (KFRP). Seven different fabric orientations were examined: 0°, 15°, 30°, 45°, 60°, 75°, and 90°. End-notched flexure (ENF) and Double cantilever beam (DCB) tests were utilized to determine modes I and II fracture toughness, respectively. Results showed that fiber orientations and fiber types have significantly affected the interface bonding between the steel and fiber-reinforced composite. For both modes I and II tests, the CFRP/steel interface exhibited the highest toughness when comparing the different tested fabric types. However, when comparing the different tested fabric orientations for GFRP/Steel, the 0° GFRP/Steel interface had the maximum toughness for modes I and II tests. All steel-composite specimens tested have shown matrix, debonding, fiber breakage, delamination, and fiber kinking using the scanning electron microscopic technique.

## 1. Introduction

Metal pipelines are the most effective pipes for oil and gas transportation. However, they are susceptible to corrosion in the harsh working environment [1–3]. Thus, many researchers have been motivated to find effective and safe alternatives for traditional steel pipes, which are light, cost-effective, and have corrosion resistance. Previous works have shown that metal-polymer hybrids pipes are the best alternatives for steel pipes [4]. The use of metal-polymer hybrids (MPHs) represents a viable solution for weight reduction, especially in the automotive industry, where emissions and fuel consumption in transports will be limited. Researchers have attributed using MPHs in the automotive industry to their optimum weight, high load-carrying capacity, and durability.

Hybrid systems using advanced alloys and composite materials fiber-reinforced polymer (Steel/FRP) fascinated substantial attention since they have a low material cost and great load-bearing capacity. This hybridization can deliver better design freedom and different potentials for efficient integration [5]. However, the fabrication process of MPHs is not an easy subject since both materials have different physical and chemical properties. These differences end up with some fabricating difficulties, for example, the imperfect bonding between conventional materials and composite materials [6]. Farahani et al. classified traditional fabricating metal-polymer hybrid components into two essential procedures [7]. The main benefits of MPHs are their exceptional lifetime, impact resistance, tolerance of damage, and flame resistance compared to conventional materials and fiber-reinforced plastics [7,8]. MPHs cope with most of the metal and polymer materials limitations. Accordingly, aluminum alloys' low thermal properties and the brittle nature of composite materials can be either glass fiber, Kevlar fibers, or graphite fibers [9,10].

Davidson et al. investigated the consequence of sequencing on the release rate of energy in composite materials. Researchers in this field have examined the energy release rates and deflections for multidirectional and unidirectional specimens using three-dimensional finite element analyses and classical laminated plate theory-based methods. They have shown that the classical plate theory-based methods could accurately calculate both the average mode ratio and the total energy release rate [11]. De Baere et al. experimentally studied modes I and II of a carbon fabric reinforced polyphenylene sulfide using the DCB setup and End Notch Flexure (ENF) test, respectively. They have realized an unstable crack-growth for carbon fabric reinforced polyphenylene sulfide. Hence, Linear Elastic Fracture Mechanics was used to determine the toughness during the crack initiation stage. The Compliance-Based Beam Method was employed to predict the toughness during the propagation stages [12]. Mildner [13] conducted a comprehensive study of hybrid materials. Aluminum and steel specimens were bonded to the GFRP and CFRP laminated composites to

* Corresponding author.

https://doi.org/10.1016/j.compstruct.2021.113740
Received 9 February 2021; Revised 9 February 2021; Accepted 14 February 2021
Available online 19 February 2021

examine the effect of fiber layup. The fabricated specimens were subjected to tensile and flexural tests. The stress–strain curve for the tested specimens similarly exhibited a nonlinear behavior. Specimens with 0° fiber orientations outpaced all-steel specimens and scored the highest strength. Zhang et al. studied the failure behavior and the mechanical properties of steel/PA66 composite hybrids fabricated using injection molding technique. They subjected the prepared specimens were to tensile, bending loading to characterize their modes I and II fracture loads. Interface properties among steel and composite were tested using end notched flexure tests and a double cantilever beam. They stated that the multiple cracks start at the midplane surface between the steel and PA66 and lead to the complete failure [6].

Liu et al. studied the mode-I fracture toughness of interlaminar interfaces with different fiber orientation angles for T800/epoxy composite specimens using experimental technique and finite element analysis. They used the data reduction scheme established on the modified beam theory to determine the mode-I fracture toughness. They demonstrated that curved laminated composite had higher mode-I fracture toughness than straight laminated composites [14]. Delamination or interlaminar failure is a critical failure mechanism and one of the most common damages in laminated composite materials [15,16]. Overall, delamination may happen under three modes. These consist of the opening mode (mode I), the sliding shear mode (mode II), and the scissoring shear mode (mode III) [17]. Many researchers had already studied the interlaminar failure in fiber-reinforced composites.

Nevertheless, it is still an active research topic since new polymers with improved mechanical properties are established daily for fiber-reinforced composites. The materials' bonding properties depend on surface roughness and surface treatment. Many processes can be employed, including; plasma exposure, mechanical abrasion, and chemical etching [10,18]. However, within this study, the effect of these processes on the interlaminar fracture toughness will not be considered, and the steel sheets and FRP layers will be bonded together with adhesive only without any pre-treatments other than using the sandpaper. These research results will be considered for pipeline applications. Based on the author's knowledge, most of the work in metal fiber laminates is focused on aerospace applications, and very few papers are considering the pipeline application. This paper investigates the effect of fiber type and fiber orientation on the mode I and mode II inter-laminar fracture toughness of Steel/FRP laminates, and results are presented from an experimental investigation.

## 2. Materials and methods

### 2.1. Material

EN10130 steel sheet with a 1.5 mm thickness was used. For fiber types' effect on the interface between steel and FRP composites, three different types of (0°/90°) woven fabrics were utilized, namely woven glass, carbon, and Kevlar fabric, as shown in Fig. 1. The EL2 epoxy resin and AT30 Slow-Hardener with a density of 1.14 g/cm$^3$ were used as the polymeric matrix. Table 1 lists the elastic constants of the employed composites.

### 2.2. Fabrication process

In this study, the hybrid material systems consist of sheet metal and glass, Kevlar, or carbon fiber-reinforced polymer. The steel sheets and FRP are bonded to each other. According to the ASTM D5528 standard, laminates need to have an even number of plies and shall be unidirectional, with delamination growth happening in the 0° direction. Therefore, the number of layers used in the FRP phase was 14 layers for the case of CFRP and 10 and 8 layers for GFRP and KFRP, respectively, so all the FRP layers will have a total thickness of 1.5 mm. For the effect of fiber orientation on the interface between steel and FRP, seven different woven glass fabric orientations were examined as follows: 0°, 15°, 30°, 45°, 60°, 75°, and 90°. The steel sheets were cut into 20 mm × 150 mm panels, and the same specimen dimensions were used for both DCB and ENF tests, as shown in Fig. 2. According to ASTM D5528 and ASTMD7905 standards, a non-adhesive insert shall be introduced at the mid-plane of the steel/FRP hybrid laminate during layup to form an initiation site for the delamination, and a thin film made of polytetrafluoroethylene (PTFE) is recommended. Steel/FRP hybrid laminates with different fabric types and orientations tested for mode I and II were fabricated utilizing a vacuum-assisted resin transfer molding machine (Fig. 3), where this technique produces parts with almost no cavities and air bubbles. In this process, the vacuum bag assists the continuous flow of low-pressure infused resin from one side to the other. It also offers the benefit of not requiring an expensive autoclave. When the epoxy resin was infused into the fabric, the steel/FRP parts were allowed to cure at room temperature. Fig. 4 shows a PTFE Teflon sheet of a 0.01 mm thick layer was inserted in the middle of the polymer-metal interface to simulate the pre-crack. A pair of piano hinge tabs were bonded to the end of each specimen that will be tested for mode I to connect them to the loading arm during the test, as shown in Figs. 4 and 5.

### 2.3. Laminate stiffness

The interface bonding of composite materials is highly dependent on the laminate stiffness. Therefore, the classical lamination theory is utilized to define the relationship between resultant forces, resultant moments, mid-surface strains, and curvature as follows:

$$\begin{Bmatrix} N \\ M \end{Bmatrix} = \begin{bmatrix} A & B \\ B & D \end{bmatrix} \begin{Bmatrix} \varepsilon^0 \\ k \end{Bmatrix} \tag{1}$$

where

$$A_{ij} = \sum_{k=1}^{N} \left[\overline{Q}_{ij}\right]_k (z_k - z_{k-1}) \tag{2}$$

$$B_{ij} = \frac{1}{2} \sum_{k=1}^{N} \left[\overline{Q}_{ij}\right]_k ({z_k}^2 - {z_{k-1}}^2) \tag{3}$$

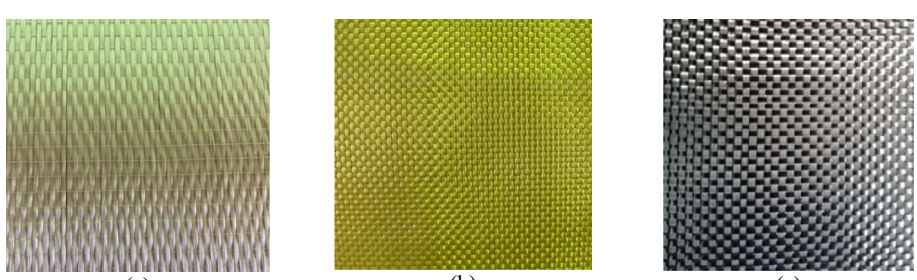

(a) (b) (c)

**Fig. 1.** (a) Woven E-Glass fabric, (b) Woven Kevlar fabric, (c) Woven carbon fabric.

**Table 1**
Elastic constants properties for GFRP, KFRP, and CFRP composites.

| $E_{11}$ (GPa) | $E_{22}$ (GPa) | $G_{12}$ (GPa) | $G_{23}$ (GPa) | $G_{13}$ (GPa) | $\nu_{12}$ | $\nu_{23}$ | $\nu_{13}$ | |
|---|---|---|---|---|---|---|---|---|
| E-Glass/Epoxy | 24.5 | 23.8 | 4.7 | 3.6 | 0.11 | 0.20 | 0.15 | 2.6 |
| Carbon/Epoxy | 77 | 75 | 6.5 | 4.1 | 0.06 | 0.37 | 0.50 | 5.1 |
| Kevlar/Epoxy | 29 | 29 | 18 | 1.8 | 0.05 | 0.11 | 0.05 | 2.2 |
| Steel | 217 | 82 | 0.28 | | | | | |

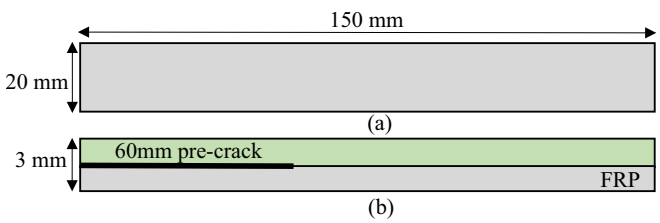


**Fig. 2.** Dimension of the DCB and ENF test specimens, a-top view, b- side view.

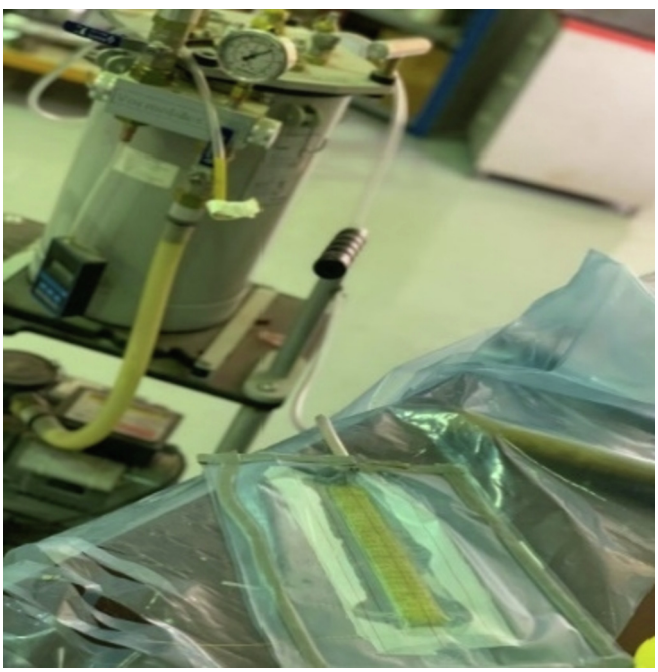

**Fig. 3.** (a) Vacuum-assisted resin transfer molding.

$$D_{ij} = \frac{1}{3}\sum_{k=1}^{N}\left[\overline{Q}_{ij}\right]_k\left(z_k{}^3 - z_{k-1}{}^3\right) \tag{4}$$

where [A] is the extensional-stiffness matrix, [B] is the extension-bending coupling matrix, [D] is the bending-stiffness matrix, i and j are the matrix notation, $z_k$ is the distance from the mid surface to the top of layer$k$, $\{N\}$ is the resultant laminate forces, $\{M\}$ is the resultant moment$\{\varepsilon^0\}$ is the mid-surface strains, $\{k\}$ is the curvature, and [Q] is the stiffness matrix.

Table 2 gives the values [A], [B], and [D] matrices. At the beginning of the mode I test, the in-plane extension-stiffness matrix plays a significant role until reaching the critical force. Then, out of plane extension-stiffness matrix takes over the propagation period, and it can be calculated using the following relations.

$$\begin{Bmatrix} Q_x \\ Q_y \end{Bmatrix} = \begin{bmatrix} A_{55} & A_{45} \\ A_{45} & A_{44} \end{bmatrix}_k \begin{Bmatrix} \gamma_{xz} \\ \gamma_{yz} \end{Bmatrix}_k \tag{5}$$

where:

$$A_{ij} = c\sum_{k=1}^{N}\left[\overline{Q}_{ij}\right]_k\left\{\left(z_k - z_{k-1}\right) - \frac{4}{3h^2}\left(z_k{}^3 - z_{k-1}{}^3\right)\right\} \tag{6}$$

where i, j = 4,5, $\gamma_{xz}$ and $\gamma_{yz}$ are out of plane shear strains, $Q_x$ and $Q_y$ are the out of plane shear forces, c is the shear correction factor, and for a rectangular section, c = 6/5 (1.2), and the total laminate thickness (h) is 3 mm [23]. The out of plane extension-stiffness matrix $A_{44}$, $A_{55}$ and $A_{45}$ values for each of the prepared specimens are recorded in Table 3. They were calculated using the following relations.

$$Q_{44} = G_{23}; \overline{Q_{44}} = Q_{44}m^2 + Q_{55}n^2 \tag{7}$$

$$Q_{55} = G_{13}; \overline{Q_{55}} = Q_{55}m^2 + Q_{44}n^2 \tag{8}$$

and

$$\overline{Q_{45}} = (Q_{55} - Q_{44})mn \tag{9}$$

where: m = cos$\theta$, and n = sin$\theta$, and $\theta$is the orientation angle.

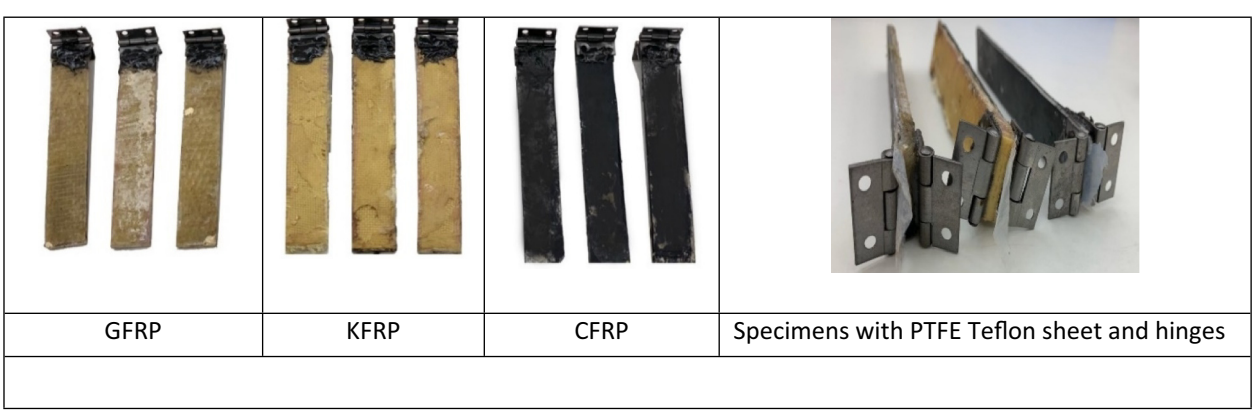


**Fig. 4.** GFRP, KFRP, and CFRP specimens for mode I test.

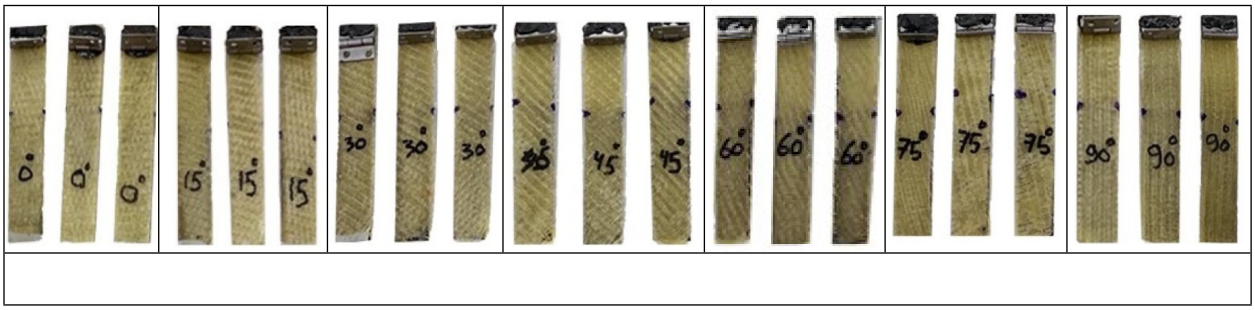


**Fig. 5.** Specimens with different fiber orientation angles for mode I test.

**Table 2**
Longitudinal stiffness matrix [A] for each prepared specimen.

| Specimens | In-plane longitudinal stiffness matrix [A] × $10^8$ (N/m) | Extension-bending coupling matrix [B] × $10^4$ (N) | Bending-stiffness matrix [D] × $10^1$ (N.m) |
|---|---|---|---|
| CFRP 0°/Steel | $\begin{bmatrix} 4.744 & 1.136 & 0.000 \\ 1.136 & 4.713 & 0.000 \\ 0.000e & 0.000 & 1.348 \end{bmatrix}$ | $\begin{bmatrix} 18.20 & 7.674 & 0.000 \\ 7.674 & 18.44 & 0.000 \\ 0.000 & 0.000 & 8.838 \end{bmatrix}$ | $\begin{bmatrix} 37.51 & 8.978 & 0.000 \\ 8.978 & 37.26 & 0.000 \\ 0.000 & 0.000 & 10.66 \end{bmatrix}$ |
| KFRP 0°/Steel | $\begin{bmatrix} 3.950 & 1.074 & 0.000 \\ 1.074 & 3.950 & 0.000 \\ 0.000 & 0.000 & 1.505 \end{bmatrix}$ | $\begin{bmatrix} 23.30 & 7.830 & 0.000 \\ 7.830 & 23.30 & 0.000 \\ 0.000 & 0.000 & 7.281 \end{bmatrix}$ | $\begin{bmatrix} 30.42 & 8.274 & 0.000 \\ 8.274 & 30.42 & 0.000 \\ 0.000 & 0.000 & 11.59 \end{bmatrix}$ |
| GFRP 0°/Steel | $\begin{bmatrix} 3.833 & 1.078 & 0.000 \\ 1.078 & 3.823 & 0.000 \\ 0.000 & 0.000 & 1.286 \end{bmatrix}$ | $\begin{bmatrix} 23.17 & 7.490 & 0.000 \\ 7.490 & 23.25 & 0.000 \\ 0.000 & 0.000 & 8.587 \end{bmatrix}$ | $\begin{bmatrix} 28.75 & 8.086 & 0.000 \\ 8.086 & 28.67 & 0.000 \\ 0.000 & 0.000 & 9.645 \end{bmatrix}$ |
| GFRP 15°/Steel | $\begin{bmatrix} 3.810 & 1.100 & 0.03988 \\ 1.100 & 3.801 & -0.03721 \\ 0.03988 & -0.03721 & 1.308 \end{bmatrix}$ | $\begin{bmatrix} 23.36 & 7.30 & -0.3245 \\ 7.30 & 23.43 & 0.3045 \\ -0.3245 & 0.3045 & 8.406 \end{bmatrix}$ | $\begin{bmatrix} 28.58 & 8.253 & 2.991 \\ 8.253 & 28.51 & -2.791 \\ 2.991 & -2.791 & 9.812 \end{bmatrix}$ |
| GFRP 30°/Steel | $\begin{bmatrix} 3.764 & 1.145 & 0.04085 \\ 1.145 & 3.759 & -0.03623 \\ 0.04085 & -0.03623 & 1.353 \end{bmatrix}$ | $\begin{bmatrix} 23.74 & 6.946 & -0.3318 \\ 6.946 & 23.78 & 0.2971 \\ -0.3318 & 0.2971 & 8.042 \end{bmatrix}$ | $\begin{bmatrix} 28.23 & 8.587 & 3.064 \\ 8.587 & 28.19 & -2.717 \\ 3.064 & -2.717 & 10.15 \end{bmatrix}$ |
| GFRP 45°/Steel | $\begin{bmatrix} 3.739 & 1.167 & 0.002668 \\ 1.167 & 3.739 & 0.002668 \\ 0.002668 & 0.002668 & 1.375 \end{bmatrix}$ | $\begin{bmatrix} 23.94 & 6.764 & -0.02001 \\ 6.764 & 23.94 & -0.02001 \\ -0.02001 & -0.02001 & 7.861 \end{bmatrix}$ | $\begin{bmatrix} 28.04 & 8.754 & 2.001 \\ 8.754 & 28.04 & 2.001 \\ 2.001 & 2.001 & 10.31 \end{bmatrix}$ |
| GFRP 60°/Steel | $\begin{bmatrix} 3.759 & 1.145 & -0.03623 \\ 1.145 & 3.764 & 0.04085 \\ -0.03623 & 0.04085 & 1.353 \end{bmatrix}$ | $\begin{bmatrix} 23.78 & 6.946 & 0.2971 \\ 6.946 & 23.74 & -0.3318 \\ 0.2971 & -0.3318 & 8.042 \end{bmatrix}$ | $\begin{bmatrix} 28.19 & 8.587 & -2.717 \\ 8.587 & 28.23 & 3.064 \\ -2.717 & 3.064 & 10.15 \end{bmatrix}$ |
| GFRP 75°/Steel | $\begin{bmatrix} 3.801 & 1.100 & -0.03721 \\ 1.100 & 3.810 & 0.03988 \\ -0.03721 & 0.03988 & 1.308 \end{bmatrix}$ | $\begin{bmatrix} 23.43 & 7.309 & 0.3045 \\ 7.309 & 23.36 & -0.3245 \\ 0.3045 & -0.3245 & 8.406 \end{bmatrix}$ | $\begin{bmatrix} 28.51 & 8.253 & -2.791 \\ 8.253 & 28.58 & 2.991 \\ -2.791 & 2.991 & 9.812 \end{bmatrix}$ |
| GFRP 90°/Steel | $\begin{bmatrix} 3.823 & 1.078 & 0.000 \\ 1.078 & 3.833 & 0.000 \\ 0.000 & 0.000 & 1.286 \end{bmatrix}$ | $\begin{bmatrix} 23.25 & 7.490 & 0.000 \\ 7.490 & 23.17 & 0.000 \\ 0.000 & 0.000 & 8.587 \end{bmatrix}$ | $\begin{bmatrix} 28.67 & 8.086 & 0.000 \\ 8.086 & 28.75 & 0.000 \\ 0.000 & 0.000 & 9.645 \end{bmatrix}$ |

**Table 3**
$A_{44}, A_{55}$ and $A_{45}$ values for each of the prepared specimens.

| Specimens | $A_{44}$ × $10^6$ (N/m) | $A_{55}$ × $10^6$ (N/m) | $A_{45}$ × $10^6$ (N/m) |
|---|---|---|---|
| Fiber type | | | |
| CFRP 0°/Steel | 7.57 | 9.42 | 0 |
| KFRP 0°/Steel | 3.69 | 4.51 | 0 |
| GFRP 0°/Steel | 6.47 | 4.67 | 0 |
| Fiber Orientation | | | |
| GFRP 0°/Steel | 6.47 | 4.67 | 0 |
| GFRP 15°/Steel | 6.35 | 4.80 | −0.40 |
| GFRP 30°/Steel | 6.02 | 5.12 | −0.40 |
| GFRP 45°/Steel | 5.57 | 5.57 | 0 |
| GFRP 60°/Steel | 5.12 | 6.02 | 0.40 |
| GFRP 75°/Steel | 4.80 | 6.35 | 0.40 |
| GFRP 90°/Steel | 4.67 | | 0 |

### 2.4. Testing procedures

Effects of fiber orientation and fiber type on the interface bonding between steel and fiber-reinforced composite were examined, and the fracture loads for modes I and II were computed. Double cantilever beam (DBC) and end-notched flexure (ENF) tests were applied to characterize mode I and mode II interlaminar fracture toughness, respectively. The unidirectional woven fabric laminates consist of 10 and 8 layers for GFRP and KFRP, respectively, and 14 layers for carbon fiber.

#### 2.4.1. Double cantilever beam (DCB) test

A double cantilever beam (DCB) test was applied to characterize mode I, the crack-opening mode, in which the delamination faces open away from each other. Fig. 6 shows a schematic illustration of the DCB sample of steel/composite hybrids. During the test, the crack progress and the initiated forces leading to delamination are measured.

Three identical specimens were tested from each fiber type and fiber orientation to assure that the results are reliable. The load was subjected vertically to the crack plane utilizing an INSTRON universal materials testing machine. The crosshead was moving at a speed of 2.5 mm/min. Cracks initiated in a stable mode, followed by some fluctuations and cracking in the matrix. The optical crack length measurement method was applied during the test, where high-quality videos were recorded for the entire test to assist the optical crack length measurement. The strain energy release rate ($G_C$) is the energy lost in the test specimens per unit of sample width for a tiny increase in delamination length for delamination growing self-similarly under a stable displacement. It is the best material property that represents the resistance to delamination. Fig. 7 shows the DCB sample, including the application of force and the crack opening progress.

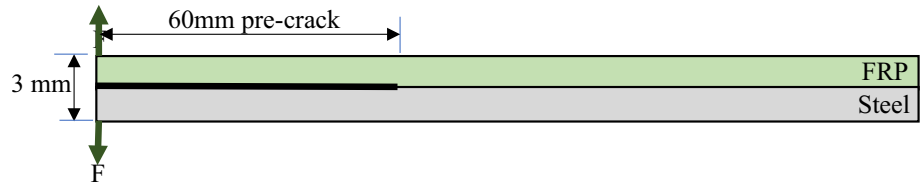


**Fig. 6.** Schematic illustration of the DCB sample of steel/composite hybrids.

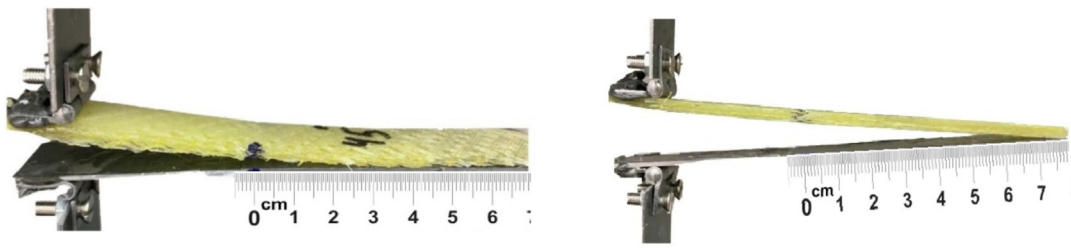

**Fig. 7.** Crack opening progress for the DCB test.

The rate of $G_{IC}$ can be determined using the Modified beam theory based on ASTM D5528, as shown in the following equation.

$$G_{IC} = \frac{3F\delta}{2ba} \tag{10}$$

where: a is the crack progress length [m], b is the sample width [m], $F$ is the critical load at [N], $\delta$ is the corresponding displacement [m].

### 2.4.2. End notched flexure (ENF) test

The FRP/steel specimens were loaded by shear forces in the crack initiation zone to define the energy release rate $G_{IIC}$ under the load according to mode II. The specimens were exposed to a 3-point bending load condition until crack propagation. The ENF test enables the shear loading of the pre-cracked specimen by compressing the mid-span of the assembly, where the shear stress is always maximum at the mid-plane, which the location of the pre-crack in the tested specimens. Fig. 8 shows a schematic illustration of the ENF set of steel/composite hybrids.

The load was applied to the specimens at a constant crosshead rate of 1.5 mm/min, where the applied displacement generated shear mode loading at the crack front. The crack length was measured similarly as in DCB tests using the optical measurement method. Fig. 9 shows the ENF sample, including force and the Bending progress. According to ASTMD7905, one can determine the energy release rate $G_{IIC}$ using Eq. (11).

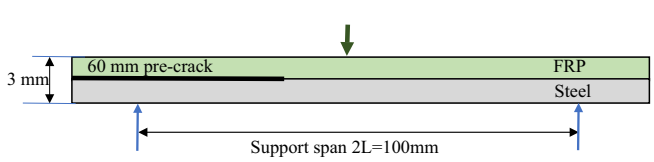


**Fig. 8.** Schematic illustration of the ENF set of steel/composite hybrids.

$$G_{IIC} = \frac{9F\delta a^2}{2b(2L^3 + 3a^3)} \tag{11}$$

where: $2L$ is the span length.

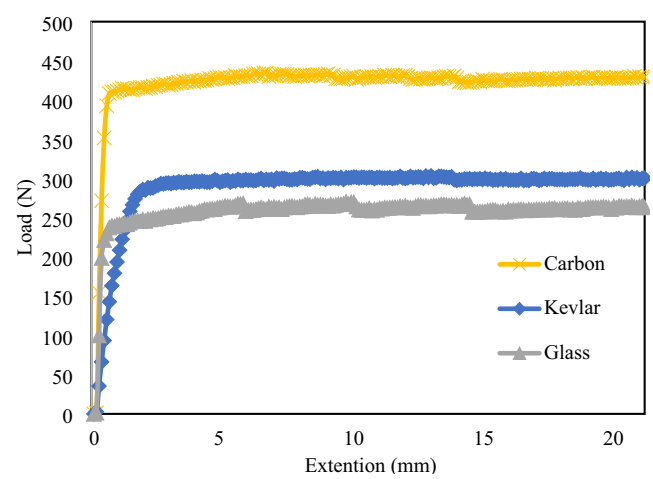


**Fig. 10.** Force-displacement curves of the DCB specimens with different fabric types.

**Table 4**
Mode I interlaminar fracture toughness $G_{IC}$ for different fabric types.

| Fabric type | $G_{IC}$ initial value [J/m$^2$] | $G_{IC}$ propagation value [J/m$^2$] |
|---|---|---|
| CFRP | 395.35 ± 1.44% | 7875.56 ± 1.67% |
| KFRP | 369.45 ± 1.11% | 5625.42 ± 1.24% |
| GFRP | 177.75 ± 1.98% | 4856.25 ± 1.85% |

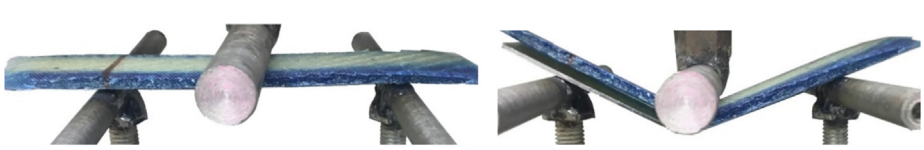

**Fig. 9.** Bending progress for the ENF test.

According to ASTMD7905, the cylindrical loading surface must have a radius, $r_1$, in the range of 4.7–9.6 mm. A steel cylinder with a radius of 8 mm was used for loading. The cylindrical supporting surfaces shall have the same radius, $r_2$, which shall be in the range of 3.0–6.4 mm. So, steel cylinders with a radius of 5 mm were used as the supports. The loading surface shall be centered between the two supporting surfaces.

## 3. Results and discussion

### 3.1. Interface properties

#### 3.1.1. Double cantilever beam (DCB) test (Mode I)

The DCB fracture test's load-extension curves for the FRP/steel specimens with different fabric types are presented in Fig. 10, where the average of each three identical specimens is plotted in the graph.

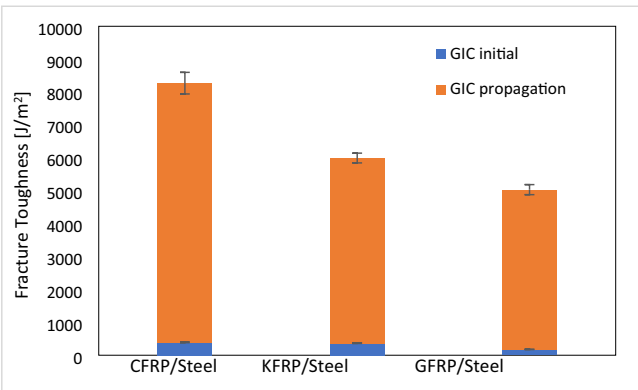


**Fig. 11.** Mode I's initial and propagation fracture toughness for specimens with different fabric types.

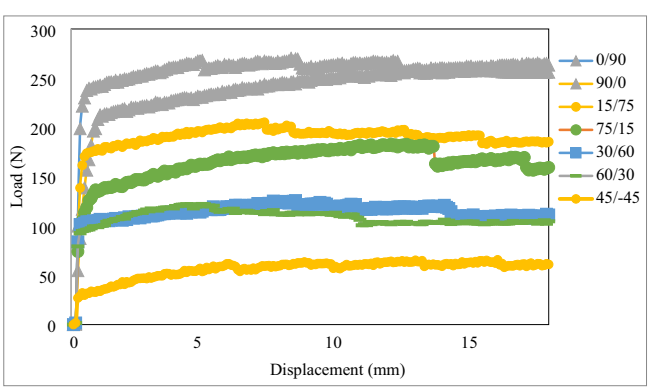


**Fig. 12.** Force-displacement curves of DCB specimens with different fabric orientation.

**Table 5**
Mode I interlaminar fracture toughness $G_{IC}$ for different fabric orientation.

| Orientation angle | $G_{IC}$ initial value [J/m$^2$] | $G_{IC}$ propagation value [J/m$^2$] |
|---|---|---|
| 0° | 177.75 ± 1.98% | 4856.25 ± 1.85% |
| 15° | 139.62 ± 2.31% | 3562.53 ± 2.24% |
| 30° | 54.10 ± 5.35% | 2137.52 ± 4.89% |
| 45° | 8.67 ± 4.19% | 1050.43 ± 3.68% |
| 60° | 50.35 ± 1.94% | 2043.75 ± 1.73% |
| 75° | 129.75 ± 2.20% | 3112.51 ± 2.51% |
| 90° | 172.28 ± 1.24% | 4537.50 ± 1.36% |

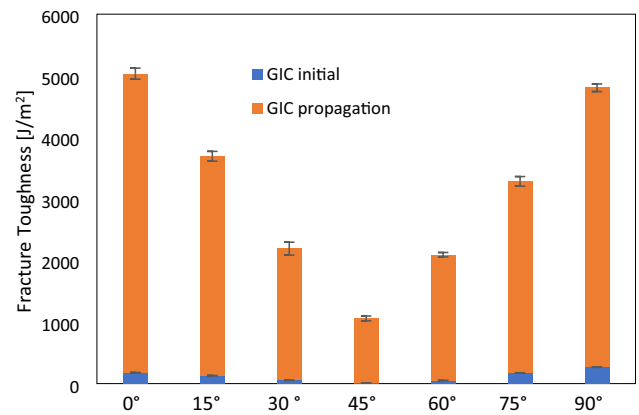


**Fig. 13.** Mode I's initial and propagation fracture toughness for specimens with different fabric types.

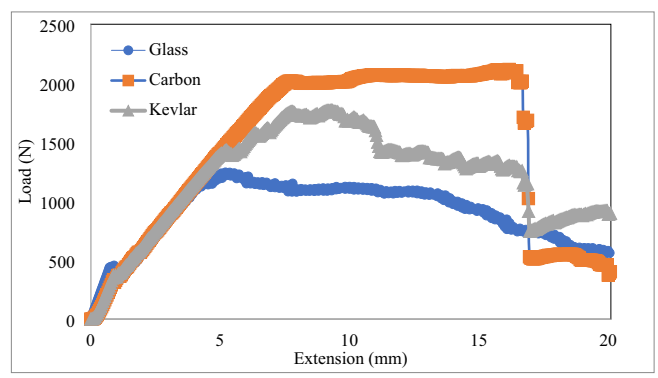


**Fig. 14.** force–displacement curves of the ENF specimens with different fabric types.

**Table 6**
Mode II interlaminar fracture toughness $G_{IIC}$ for different fabric types.

| Fabric type | $G_{IIC}$ initial value [J/m$^2$] | $G_{IIC}$ propagation value [J/m$^2$] |
|---|---|---|
| CFRP | 294.80 ± 2.41% | 20189.03 ± 2.89% |
| KFRP | 254.46 ± 3.55% | 18544.23 ± 3.12% |
| GFRP | 239.48 ± 2.25% | 14125.87 ± 2.47% |

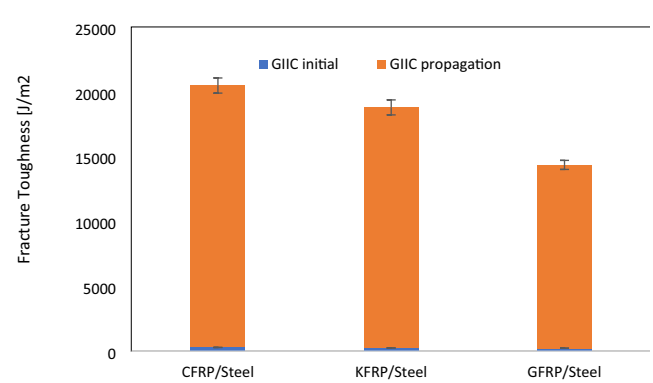


**Fig. 15.** Comparison of the mode II initial and propagation fracture toughness for specimens with different fabric types.

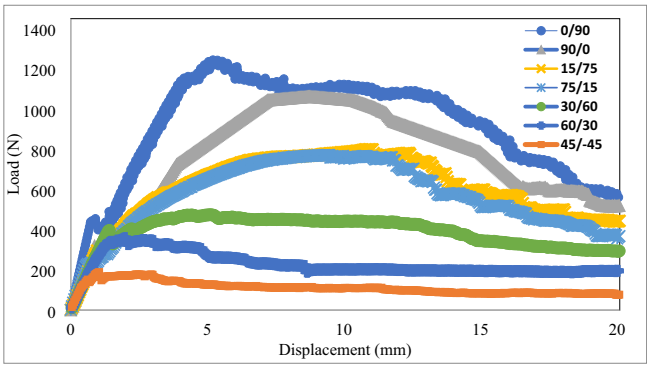


**Fig. 16.** Load-displacement curves of the ENF specimens with different fabric orientation.

**Table 7**
Mode II interlaminar fracture toughness $G_{IIC}$ for different fabric orientation.

| Orientation angle | $G_{IIC}$ initial value [J/m$^2$] | $G_{IIC}$ propagation value [J/m$^2$] |
|---|---|---|
| 0° | 239.48 ± 2.25% | 14125.87 ± 2.47% |
| 15° | 224.94 ± 2.40% | 9868.75 ± 3.45% |
| 30° | 194.11 ± 3.84% | 6434.04 ± 2.16% |
| 45° | 81.23 ± 2.02% | 1806.04 ± 1.89% |
| 60° | 161.39 ± 1.60% | 3773.34 ± 2.76% |
| 75° | 198.79 ± 3.84% | 9578.49 ± 1.57% |
| 90° | 229.98 ± 2.27% | 12593.95 ± 1.48% |

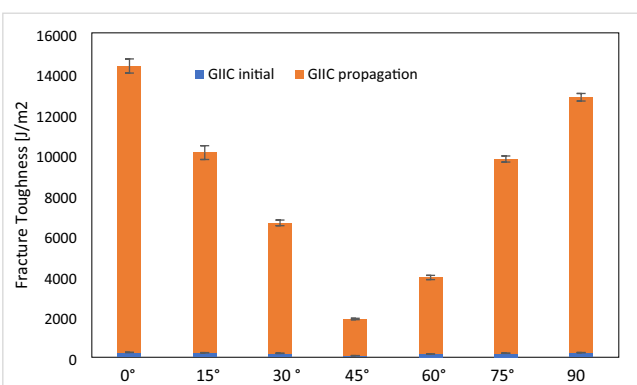


**Fig. 17.** Comparison of the mode II initial and propagation fracture toughness for specimens with different fabric orientations.

It could be observed that all the specimens have almost the same behavior. The curves show that the specimens have a linear behavior until the critical force values were reached. Those force values were used to determine the initial interlaminar fracture toughness using Eq. (10). After which, the curves showed a stable behavior with minimal fluctuations. These fluctuations are caused by fracture resistance and are associated with decreased strength. CFRP part handled the highest force value, by around 420 N, followed by KFRP parts and the GFRP parts.

Table 4 shows the effect of using different fabric types on mode I interlaminar fracture toughness$G_{IC}$. The average values for different fabric types were presented with the coefficient of variation (CoV), which is the standard deviation ratio to the mean. Three identical specimens were tested for each fabric orientation, and the recorded $G_{IC}$ values for each group indicated that the test results are reliable where the force–displacement curves of the identical specimens were overlapping each other well. It was shown that the specimens made of Steel-CFRP were the specimens that had the highest fracture toughness, where $G_{IC}$ initial and propagation values reached more than 395 and 7800 J/m$^2$ respectively. This finding is due to the high bonding strength in Steel-CFRP specimens where it was proved from the calculations in Table 2 that the Steel-CFRP specimens have the highest $A_{11}$ values, followed by the Kevlar and then glass fibers, which supports the experimental results. Fig. 11 shows a comparison between the initial and propagation fracture toughness for specimens with different fabric types.

Fig. 12 shows the DCB fracture test's load-extension curves for the GFRP/steel specimens with different fabric orientations. It can be seen from the graph that before the onset of delamination growth, the load increases linearly with applied displacement. Upon reaching the critical force point, which differs from one specimen to another, the load rises slowly as the crack progresses, demonstrating that long path crack propagation occurs. Specimens with 0° fiber orientation reached the highest forces values (around 270 N).

Table 5 demonstrates the effect of using different fabric orientation angles on mode I interlaminar fracture toughness $G_{IC}$ of the mode I fracture specimens. Mode I interlaminar fracture toughness $G_{IC}$ average values for different fabric orientation angles were computed and presented with CoV. Three identical specimens were tested for each fabric orientation, and the recorded $G_{IC}$ values for each group indicated that the test results are reliable. It shows that the specimens with 0° fabric orientation were the specimens that had the highest fracture toughness where the initial and propagation fracture toughness values reached more than 177 and 4850 J/m$^2$, respectively. This finding shows that using a 0° fabric orientation results in high bond strength of Steel/GFRP specimens. Fig. 13 shows a comparison between the mode I initial and propagation fracture toughness for specimens with different fabric orientations.

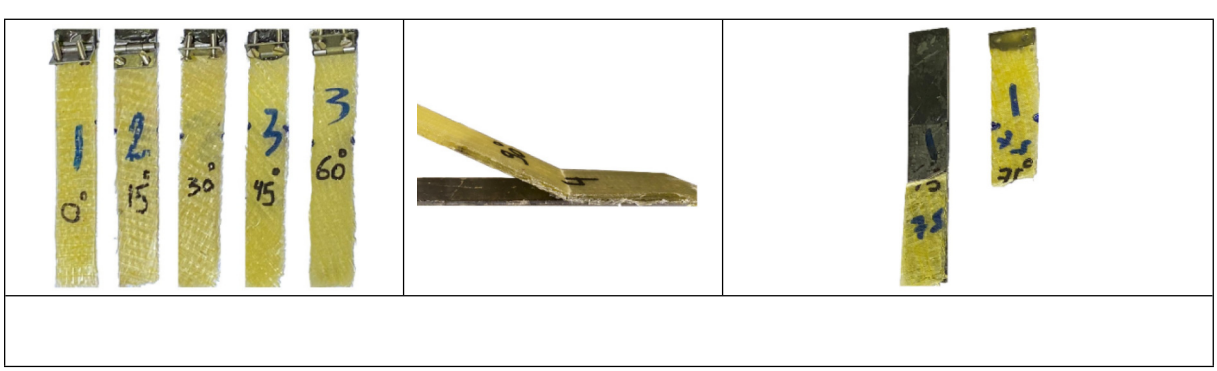

**Fig. 18.** Illustration of typical macroscopic post-failure mode for the KFRP composites with fiber orientation of 90°.

**Table 8**
Apparent Engineering constants and engineering elastic constants for each specimen.

| Specimens | $E_x$ (GPa) | $E_y$ (GPa) | $G_{xy}$ (GPa) | $\upsilon_{xy}$ | $\upsilon_{yx}$ | $a_{11}$ (GPa) | $a_{22}$ (GPa) | $a_{12}$ (GPa) | $a_{66}$ (GPa) |
|---|---|---|---|---|---|---|---|---|---|
| CFRP 0°/Steel | 121.2 | 119.3 | 19.97 | 0.161 | 0.158 | 0.0083 | 0.0084 | −0.00132 | 0.0501 |
| KFRP 0°/Steel | 68.95 | 68.95 | 34.47 | 0.168 | 0.168 | 0.0145 | 0.0145 | −0.00244 | 0.0290 |
| GFRP 0°/Steel | 62.70 | 61.79 | 17.38 | 0.205 | 0.202 | 0.0159 | 0.0162 | −0.00327 | 0.0575 |
| GFRP 15°/Steel | 58.33 | 57.64 | 18.93 | 0.26 | 0.256 | 0.0171 | 0.0173 | −0.00444 | 0.0528 |
| GFRP 30°/Steel | 51.16 | 50.86 | 23.05 | 0.348 | 0.346 | 0.0195 | 0.0197 | −0.00680 | 0.0434 |
| GFRP 45°/Steel | 48.12 | 48.12 | 25.86 | 0.384 | 0.384 | 0.0208 | 0.0208 | −0.00798 | 0.0387 |
| GFRP 60°/Steel | 50.86 | 51.16 | 23.05 | 0.346 | 0.348 | 0.0197 | 0.0195 | −0.00680 | 0.0434 |
| GFRP 75°/Steel | 57.64 | 58.33 | 18.93 | 0.256 | 0.26 | 0.0173 | 0.0171 | −0.00446 | 0.0528 |
| GFRP 90°/Steel | 61.79 | 62.70 | 17.38 | 0.202 | 0.205 | 0.0162 | 0.0159 | −0.00327 | 0.0575 |

**Table 9**
Stress intensity factors, Modes I and II, effective moduli.

| Specimens | $E_I$ (GPa) | $E_{II}$ (GPa) | $G_I$ initial | $G_{II}$ initial | $K_I$ (MPa)$\sqrt{m}$ | $K_{II}$ (MPa)$\sqrt{m}$ |
|---|---|---|---|---|---|---|
| Effect of fiber types | | | | | | |
| CFRP 0°/Steel | 169.00 | 171.0 | 395.35 | 294.8 | 8.18 | 7.09 |
| KFRP 0°/Steel | 97.50 | 97.5 | 369.45 | 254.46 | 6.00 | 4.98 |
| GFRP 0°/Steel | 87.70 | 88.3 | 177.75 | 239.48 | 3.95 | 4.59 |
| Effect of fiber orientation | | | | | | |
| GFRP 0°/Steel | 87.70 | 88.30 | 177.75 | 239.48 | 3.95 | 4.59 |
| GFRP 15°/Steel | 81.80 | 82.20 | 139.62 | 224.94 | 3.38 | 4.30 |
| GFRP 30°/Steel | 72.00 | 72.20 | 54.10 | 194.11 | 1.97 | 3.74 |
| GFRP 45°/Steel | 68.10 | 68.10 | 8.67 | 81.23 | 0.77 | 2.35 |
| GFRP 60°/Steel | 72.20 | 72.00 | 50.35 | 161.39 | 1.91 | 3.40 |
| GFRP 75°/Steel | 82.20 | 81.80 | 129.75 | 198.79 | 3.27 | 4.03 |
| GFRP 90°/Steel | 88.30 | 87.70 | 172.28 | 229.98 | 3.90 | 4.49 |

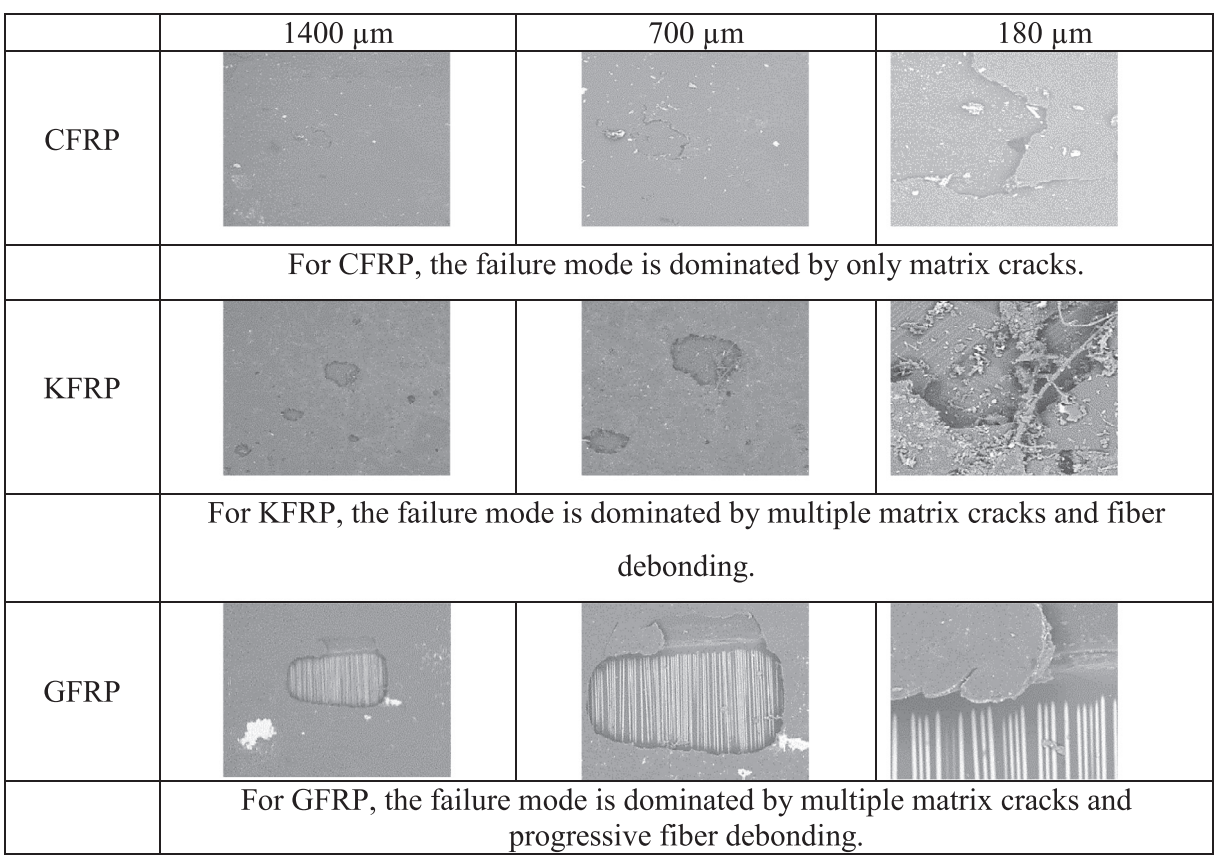


**Fig. 19.** SEM images for mode I test specimens with different fabric types.

The above experimental data of the DCB fracture test matches the classical lamination theory results in Section 2.3. Based on the classical lamination theory, extensional stiffness affects the composite materials' response to the applied load. One can conclude that the CFRP/steel laminate will have a minimal mid-plane strain for a given resultant force since the elements of its [A] matrix were the highest when compared to other laminate matrices. Terms $A_{16}$ and $A_{26}$ couple shear and normal responses of the laminate. It could be noticed from Table 2 that all GFRP/steel laminates with an orientation other than $0^{\circ}$ have nonzero values for $A_{16}$ and $A_{26}$. Therefore, a resultant extensional force on those laminates will generate extensional strain and shear strain. Second, when the Extension-bending coupling matrices are analyzed, it could be noted that all [B] matrices are nonzero since all the laminates are not symmetric, knowing that this matrix couples extensional response to the bending response of the laminate. The nonzero [B] matrix means that all the above laminates will experience extension and shear deformations and bending–twisting curvatures in mode-I when subjected to the normal force.

### 3.1.2. ENF test

Fig. 14 shows the force–displacement curves of the ENF specimens with different fabric types. As can be seen, the FRP/steel specimens with different fabric types show an overall linear response in the first portion of the graph until reaching the critical force's values, where

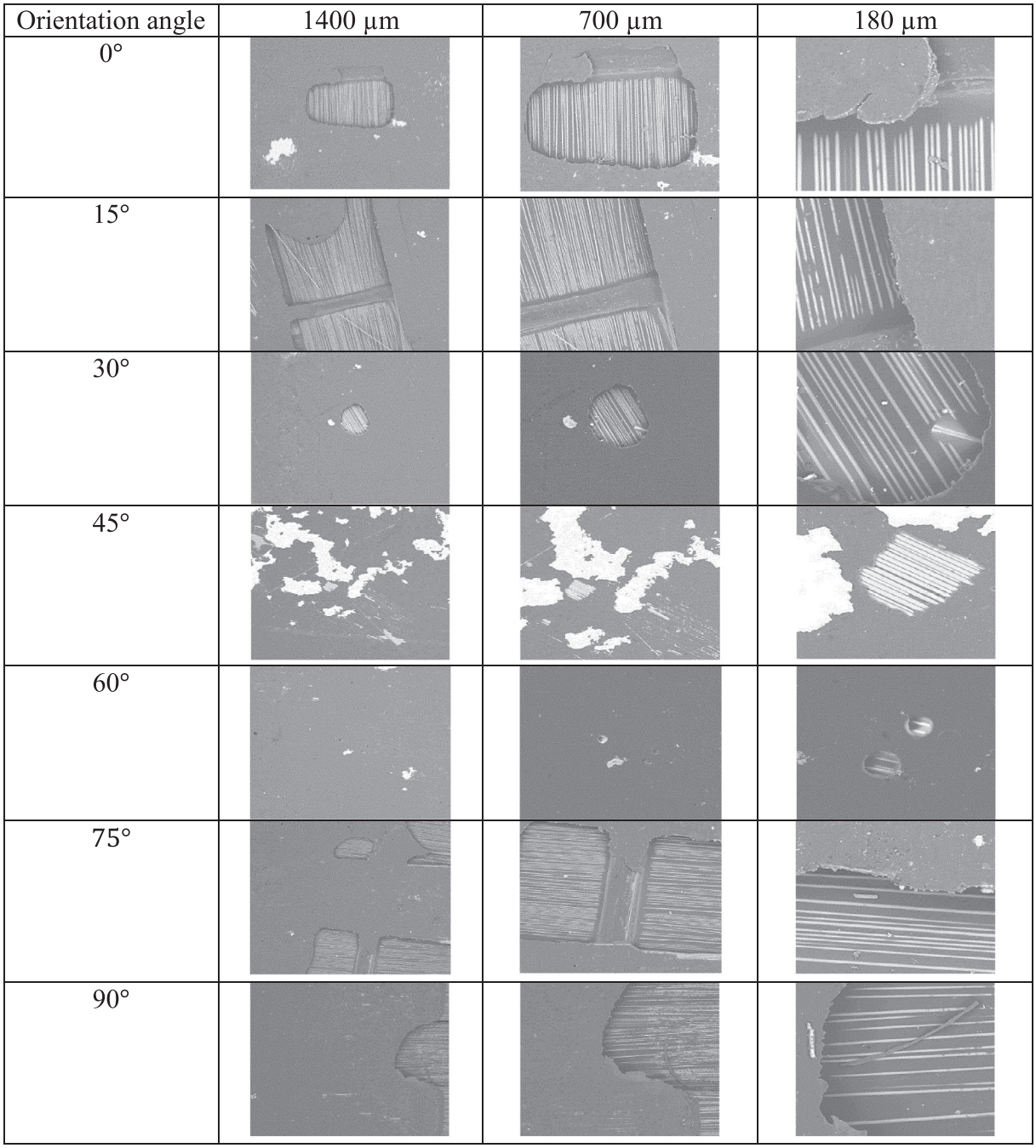


**Fig. 20.** SEM images for mode I test specimens with different orientation angles. The domination failure mode is associated with multiple matrix cracks, progressive fiber debonding, and fiber breakage.

those values were used to determine the initial interlaminar fracture toughness using Eq. (11). Then the curves continued rising until the peak loads were recorded. CFRP parts reached the higher forces values by around 2000 N. Then, a clear and sudden load drop was observed. This is expected behavior since the mid-plane surfaces slide over each other, leading to fast crack growth and sudden load drop when subjected to an in-plane shear loading. KFRP and GFRP parts behavior were slightly different where the load values kept fluctuating and decreasing gradually until failure, which indicates that they exhibited much slower crack growth with more stable loading responses during the test.

Table 6 demonstrates the effect of using different fabric types on the total energy absorbed during testing mode II interlaminar fracture specimens. The force–displacement curves of the identical specimens overlapped each other well, which proves that the results are reliable. It was shown that the specimens made of steel-CFRP were the specimens that had the highest fracture toughness, where $G_{IIC}$ initial and propagation values reached more than 290 and 20000 J/m$^2$ respectively. This fact reveals that Steel-CFRP specimens have good interface properties. Fig. 15 shows a Comparison between the mode II initial and propagation fracture toughness for specimens with different fabric types.

The mode II loading behavior of the FRP/steel specimens with different fabric orientation is plotted in Fig. 16. All the ENF specimens display similar and consistent responses, as shown in their load–displacement curves. The specimens reveal an early linear behavior followed by a nonlinear curve up to the peak load. A slow load decrease can be noticed until the test end, where the gradual decrease in force is associated with a decrease in strength. When a decrease in the load rate is noticed, the specimen's stiffness decreases. Specimens with 0° fiber orientation reached the highest forces values (around 1200 N).

Table 7 demonstrates the effect of using different fabric orientation angles on the overall energy absorbed throughout mode II interlaminar fracturing. $G_{IIC}$ average values for different fabric types were computed and presented with CoV. It was shown that the specimens with 0° fabric orientation had the highest fracture toughness in which the $G_{IIC}$ initial and propagation values reached more than 230 and 14,000 J/m$^2$ respectively. This finding shows that using 0° fabric orientation results in high bond strength of Steel/GFRP specimens. Fig. 17 shows a comparison between the mode II initial and propagation fracture toughness for specimens with different fabric orientations.

The above experimental data of the ENF fracture test matches the classical lamination theory results in Section 2.3. All the extension-bending coupling matrices for all specimens in Table 2 are nonzero since no laminates are symmetric. This means that all the laminates will create bending and twisting curvatures and extension-shear deformations in mode II when subjected to bending moment. Furthermore, looking at the bending-stiffness matrices in Table 2, this matrix influ-

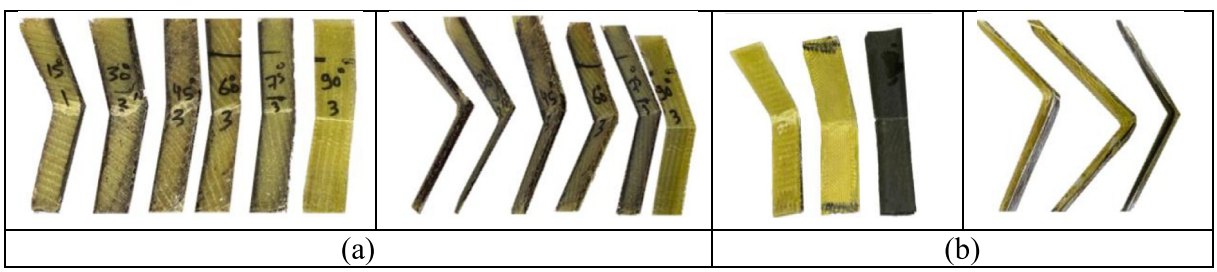


**Fig. 21.** Post failure images for mode II test specimens, a- different orientation angles, b- different fabric type.

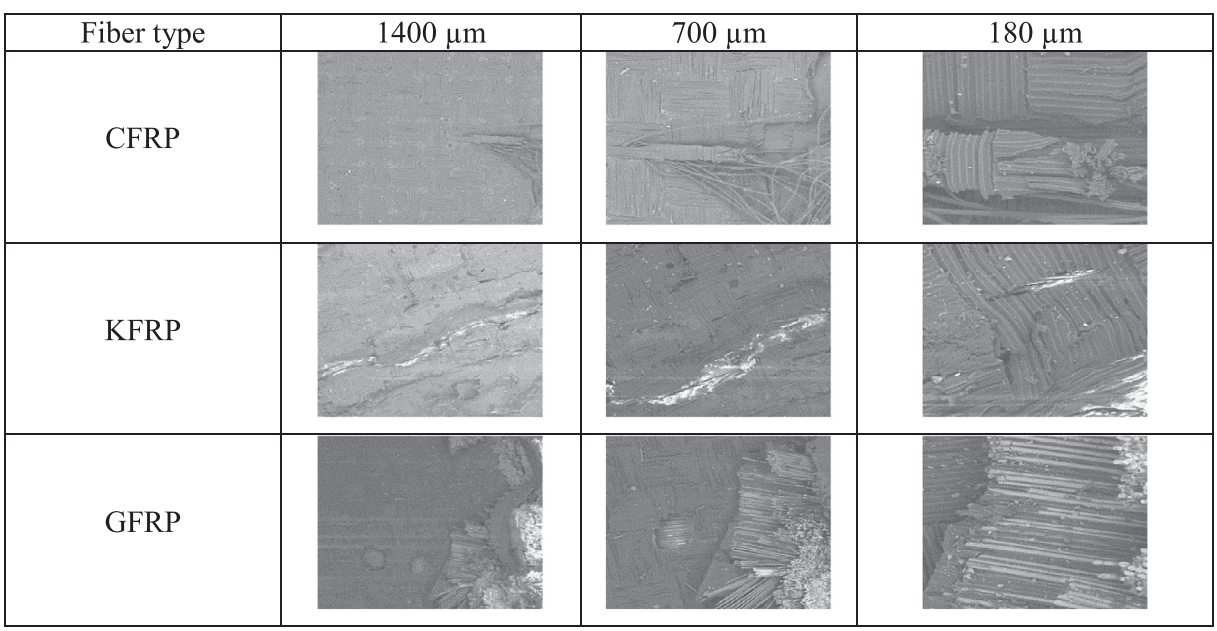


**Fig. 22.** SEM images for mode II test specimens with different fabric types. The failure mode is dominated by matrix cracks, fiber debonding, delamination, and fiber breakage for CFRP. For KFRP, the failure mode is dominated by multiple matrix cracks and fiber kinking. For GFRP, the failure mode is dominated by multiple matrix cracks, progressive fiber debonding, delamination, and progressive fiber breakage.

ences a laminate's bending response. It could be concluded that the CFRP/steel laminate will generate less curvature when subjected to bending moment since it has the most considerable magnitude of [D] matrix. Terms $D_{16}$ and $D_{26}$ coupled bending and twisting responses of the laminate. It is observed that all GFRP/steel laminates with an orientation other than $0^{\circ}$ have nonzero values for $D_{16}$ and $D_{26}$. Thus, the pure bending moment will generate bending curvature and twist curvature in all of the previously mentioned laminates. Likewise, by analyzing the data in Table 3, it could be observed that CFRP/steel laminate has the highest $A_{44}$ and$A_{55}$ values, which predicts that when subjected to shear forces, minimal out of plane shear strains will be generated while KFRP/steel laminates will have the highest plane shear strain values. Based on experimental data, the results indicate that when the laminates are subjected to loading, it fails earlier in Mode-I load compared to Mode-II loading.

### 3.2. Stress intensity factor

Prediction of composite materials' delamination is one of the main challenges to promote the interface between composite and other materials. One useful technique to examine the interlaminar cracks in composite materials is the linear elastic fracture mechanics (LEFM) [19]. The FRP specimens are assumed to be made of an orthotropic material. Therefore, the strain–stress relation is defined using the generalized Hooke's law as follows:

$$\begin{Bmatrix} \varepsilon_x \\ \varepsilon_y \\ \varepsilon_z \\ \gamma_{yz} \\ \gamma_{xz} \\ \gamma_{xy} \end{Bmatrix} = \begin{bmatrix} a_{11} & a_{12} & a_{13} & 0 & 0 & 0 \\ a_{21} & a_{22} & a_{23} & 0 & 0 & 0 \\ a_{31} & a_{32} & a_{33} & 0 & 0 & 0 \\ 0 & 0 & 0 & a_{44} & 0 & 0 \\ 0 & 0 & 0 & 0 & a_{55} & 0 \\ 0 & 0 & 0 & 0 & 0 & a_{66} \end{bmatrix} \begin{Bmatrix} \sigma_x \\ \sigma_y \\ \sigma_z \\ \tau_{yz} \\ \tau_{xz} \\ \tau_{xy} \end{Bmatrix} \tag{12}$$

In which one can write the engineering elastic constants as follows:

$$\begin{aligned} a_{11} &= \frac{1}{E_x}, \quad a_{12} = -\frac{\vartheta_{yx}}{E_y}, \quad a_{13} = -\frac{\vartheta_{zx}}{E_z} \\ a_{21} &= -\frac{\vartheta_{xy}}{E_x}, \quad a_{22} = \frac{1}{E_y}, \quad a_{23} = -\frac{\vartheta_{zy}}{E_z} \\ a_{31} &= -\frac{\vartheta_{xz}}{E_x}, \quad a_{32} = -\frac{\vartheta_{yz}}{E_y}, \quad a_{33} = \frac{1}{E_z} \\ a_{44} &= \frac{1}{G_{yz}}, \quad a_{55} = \frac{1}{G_{xz}}, \quad a_{66} = \frac{1}{G_{xy}} \end{aligned} \tag{13}$$

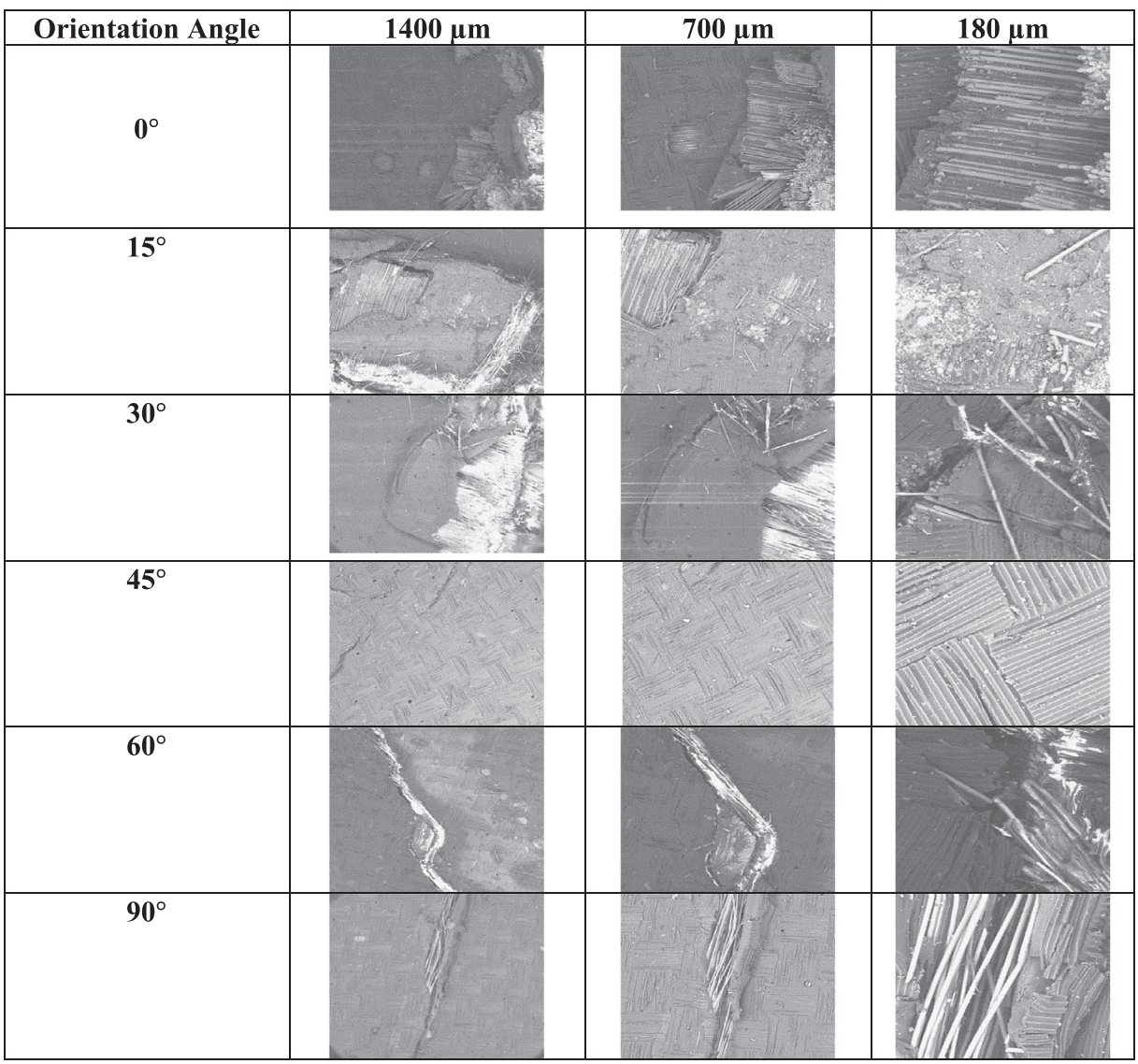


**Fig. 23.** SEM images for mode II test specimens with different orientation angles. The failure mode is dominated by multiple matrix cracks, progressive fiber debonding, delamination, and progressive fiber breakage.

$$\frac{1}{E_x} = \frac{m^4}{E_1} + \left(\frac{1}{G_{12}} - \frac{2\vartheta_{12}}{E_1}\right)m^2n^2 + \frac{n^4}{E_2} \tag{14}$$

and,

$$\frac{1}{E_y} = \frac{n^4}{E_1} + \left(\frac{1}{G_{12}} - \frac{2\vartheta_{12}}{E_1}\right)m^2n^2 + \frac{m^4}{E_2} \tag{15}$$

$$\frac{1}{G_{xy}} = 2m^2n^2\left(\frac{2}{E_1} + \frac{2}{E_2} + \frac{4\vartheta_{12}}{E_1} - \frac{1}{G_{12}}\right) + \frac{(n^4 + m^4)}{G_{12}} \tag{16}$$

where xyz is the global directions, 123 are the principal material directions, m = cos$\theta$, and n = sin$\theta$. The values for $E_1$, $E_2$, $G_{12}$ and $\upsilon_{12}$ were listed in Table 1. The calculated engineering elastic constants are listed in Table 8.

The relationships for an orthotropic material's energy release rates will be utilized to define the stress intensity factors for mode I and mode II of each specimen [19]. The stress intensity factor depends on specimen geometry, the crack's size and location, and the magnitude and distribution of loads on the material [20].

$$G_I = \frac{K_I^2}{E_I}, G_{II} = \frac{K_{II}^2}{E_{II}} \tag{17}$$

where, $E_I$ and $E_{II}$ are the effective moduli for modes I and II. One can calculate the effective moduli as follows:

$$E_I = \sqrt{\frac{2}{a_{11}a_{22}}}\frac{1}{\sqrt{\sqrt{\frac{a_{22}}{a_{11}}} + \frac{2a_{12}+a_{66}}{2a_{11}}}}, \; E_{II} = \frac{\sqrt{2}}{a_{11}}\frac{1}{\sqrt{\sqrt{\frac{a_{22}}{a_{11}}} + \frac{2a_{12}+a_{66}}{2a_{11}}}} \tag{18}$$

$K_I$ and $K_{II}$ are stress intensity for modes I and II, respectively [21,22].

$G_I$ and $G_{II}$ are the fracture toughness for modes I and II, respectively.

Table 9 lists the calculated effective moduli and stress intensity factors using Eqs. (17) and (18). So as $K_I$ and $K_{II}$ values increase, the resistance to fracture will also increase. One can notice that CFRP/Steel specimens have the highest resistance to fracture than the other tested fabric types. While for the different orientation angles in GFRP/Steel, the specimens with 0° and 90° orientation angles have the highest resistance to modes I and II, respectively.

### 3.3. Failure surfaces of mode I and mode II interlaminar fracture

All modes of failure and the interlaminar fracture surfaces were identified using the SEM. All the failure modes of the modes I and II interlaminar fracture specimens were classified and presented in Figs. 19, 20, 22, and 23, respectively, with three different scales (1400 μm, 700 μm, and 180 μm) using the microscopic investigations via scanning electron microscopy. The fractured surfaces were coated with Gold palladium/platinum coating in the fine auto coater to make the polymer surface conductive.

#### 3.3.1. Mode-I interlaminar failure surfaces

Fig. 18 shows post-failure images for the specimens that were tested for mode I; some specimens experienced full separation between the steel and composite layer without any breakage, while other specimens experienced full separation in the area of the Teflon layer. The composite layer then starts to break completely in the area where the adhesion between layers is vital, as shown in the following images.

For mode-I fracture, the SEM specimens were taken from the crack initiation area beyond the pre-crack insert film. The fractography of all the steel-composite specimens tested for mode I reveal that they have established some cracking, fiber–matrix debonding, and peeling off for the resin matrix layer in some sheet areas; some fiber failure and breakage of the applied tensile loads were detected using SEM. The SEM images of fractured surfaces of GFRP specimens with different fabric orientations were observed; each fracture type was labeled in the figures. The surface shows the broken fibers, pull-out, and matrix peeling caused by Mode-I loading. Usually, throughout delamination, matrix shear yielding happens in resin-rich areas by stretching the neighboring fibers causing a higher energy absorption [23]. This failure mechanism was detected in many specimens.

#### 3.3.2. Mode-II interlaminar failure surfaces

Fig. 21 shows post-failure images for the specimens tested for mode II. All steel-composite specimens tested for mode II have caused multiple matrix cracks and debonding between the fiber and the matrix, accompanied by fiber fracture attributed to the flexural loads, which was also examined using SEM. One can observe that the fiber breakage region was located near the point flexural load, as shown in Figs. 22 and 23.

Scanning electron microscopy images of the fracture area near the mode-II GFRP specimen's crack tip with different fabric orientation are shown in Fig. 23. All over the specimens' fracture surface, broken fibers were observed following the fiber–matrix debonding in the vicinity of the series of matrix cracks. It is also interesting to note that progressive debonding between fiber and matrix failures are in areas of the matrix deformation among adjacent fibers that are elevated parallel to one another and tend to incline in the same direction over the whole surface. Similar failure modes are identified by other researchers [24,25].

## 4. Conclusion

The present study investigates the fiber type and fiber orientation's effects on the interface bonding between steel and fiber-reinforced composites. The fracture loads for modes I and II were computed using DCB and ENF tests. The outcomes of this study are listed below:

1. The interface bonding between the steel and fiber-reinforced composite and the modes I and II fracture toughness had been significantly affected by fiber orientation and fiber types.
2. For both modes I and II tests, the CFRP/steel interface exhibited the highest toughness when comparing the different tested fabric types. However, when comparing the effect of fiber orientations, the 0° GFRP/Steel interface had the maximum toughnesses for mode I and mode II tests.
3. It is well observed that all specimens' delamination response strongly depends on the loading condition. The shearing-mode (mode II) fracture toughness is larger than the opening-mode (mode I) fracture toughness in all the tested specimens, proving that the interface between FRP and steel layer is stronger in mode II than in mode I due to the compaction process during the bending loading. While in mode I, the loading process is opening.
4. All steel-composite specimens tested for mode I have established some cracking and peeling off for the resin matrix layer in some sheet areas, followed by some fiber failure and breakage.
5. All steel-composite specimens tested for mode II have experienced matrix cracks and fiber–matrix debonding, followed by fiber failure and breakage due to the applied bending loads.

## Declaration of Competing Interest

The authors declare that they have no known competing financial interests or personal relationships that could have appeared to influence the work reported in this paper.

## References

[1] Al-Abtah FG, Mahdi E, Gowid S. The use of composite to eliminate the effect of welding on the bending behavior of metallic pipes. Compos Struct 2020;235:111793.
[2] Farag MH, Mahdi E. New approach of pipelines joining using fiber reinforced plastics composites. Compos Struct November 2019;228(15):111341.

[3] Eliyan FF, Icre F, Alfantazi A. Passivation of HAZ s of API-X 100 pipeline steel in bicarbonate-carbonate solutions at 298 K. Mater Corros 2014;65(12):1162–71.
[4] Haider D, Krahl M, Koshukow W, Wolf M, Liebsch A, Kupfer R, Gude M. Adhesion studies of thermoplastic fibre-plastic composite hybrid components Part 2: thermoplastic-metal-composites; 2018.
[5] Al-Abtah FG, Al-Huniti N, Mahdi E. Simulation-based parametric study for the hybrid superplastic forming of AZ31. Procedia Comput Sci 2019;158:177–97.
[6] Zhang Y, Sun L, Li L, Huang B, Wang T, Wang Y. Direct injection molding and mechanical properties of high strength steel/composite hybrids. Compos Struct 2019;210:70–81.
[7] Farahani S, Yerra VA, Pilla S. Analysis of a hybrid process for manufacturing sheet metal-polymer structures using a conceptual tool design and analytical-numerical modeling. J Mater Process Technol 2020;279:116533.
[8] Samer Gowid, Elsadig Mahdi, Fatima Alabtah. Modeling and optimization of the crushing behavior and energy absorption of plain-weave composite hexagonal quadruple ring systems using artificial neural network, Compos Struct 229: 2019; 111473. ISSN 0263-8223.
[9] Alderliesten RC. Designing for damage tolerance in aerospace: a hybrid material technology. Mater Des 2015;66:421–8.
[10] Laban O, Mahdi E. Enhancing mode-I inter-laminar fracture toughness of aluminum/fiberglass fiber-metal laminates by combining surface pre-treatments. Int J Adhes Adhes 2017;78:234–9.
[11] Davidson BD, Krüger R, König M. Three-dimensional analysis of center-delaminated unidirectional and multidirectional single-leg bending specimens. Compos Sci Technol 1995;54(4):385–94.
[12] De Baere I, Jacques S, Van Paepegem W, Degrieck J. Study of the Mode I and Mode II interlaminar behavior of a carbon fabric reinforced thermoplastic. Polym Test 2012;31(2):322–32.
[13] Mildner C. Numerical and experimental investigations of the crash behavior of FRP-reinforced metal structural components Ph.D. dissertation. Technical University of Munich; 2013.
[14] Liu C, Bai R, Lei Z, Di J, Dong D, Gao T, et al. Study on mode-I fracture toughness of composite laminates with curved plies applied by automated fiber placement. Mater Des 2020;195:108963.
[15] Shokrieh MM, Zeinedini A, Ghoreishi SM. On the mixed-mode I/II delamination R-curve of E-glass/epoxy laminated composites. Compos Struct 2017;171:19–31.
[16] Jahanian E, Zeinedini A. Influence of drilling on mode II delamination of E-glass/epoxy laminated composites. Theor Appl Fract Mech 2018;96:398–407.
[17] Moradi E, Zeinedini A. On the mixed mode, I/II/III inter-laminar fracture toughness of cotton/epoxy laminated composites. Theor Appl Fract Mech 2020;105:102400.
[18] Kurtovic A, Brandl E, Mertens T, Maier HJ. Laser-induced surface nano-structuring of Ti–6Al–4V for adhesive bonding. Int J Adhes Adhes 2013;45:112–7.
[19] Choupani N. Experimental and numerical investigation of the mixed-mode delamination in Arcan laminated specimens. Mater Sci Eng, A 2008;478 (1–2):229–42.
[20] Fantuzzi N, Dimitri R, Tornabene F. A SFEM-based evaluation of mode-I Stress Intensity Factor in composite structures. Compos Struct 2016;145:162–85.
[21] ASTM E399, Standard Test Method for Plane Strain Fracture Toughness and Strain Energy Release Rate of Metallic Materials: Annual Book of ASTM Standards; 1983
[22] Reissner E. The effect of transverse shear deformation on the bending of elastic plates. J Appl Mech 1945:A69–77.
[23] Saravanakumar K, Nibras Farouk, Arumugam V. Effect of fiber orientation on Mode-I delamination resistance of glass/epoxy laminates incorporated with milled glass fiber fillers. Eng Fract Mech 199: 2018; 61–70.
[24] Reeder JR. An Evaluation of Mixed-mode Delamination Failure Criteria, National Aeronautics and Space Administration Langley Research Center Hampton, Virginia 23665-5225, Nasa Technical Memorandum 104210,1992.
[25] Reza Mohammadi, Mehdi Ahmadi Najafabadi, Hamed Saghafi, Dimitrios Zarouchas. Mode-II fatigue response of AS4/8552 carbon/epoxy composite laminates interleaved by electrospun nanofibers. Thin-Walled Struct 154: 2020; 106811